A&A 663, L6 (2022)
https://doi.org/10.1051/0004-6361/202244068


Astronomy & Astrophysics

LETTER TO THE EDITOR

# Mapping 'out-of-the-box' the properties of the baryons in massive halos

M. Angelinelli[1,2], S. Ettori[2,3], K. Dolag[4,5], F. Vazza[1,6,7], and A. Ragagnin[1,8,9]

[1] Dipartimento di Fisica e Astronomia, Universitá di Bologna, Via Gobetti 92/3, 40121 Bologna, Italy
e-mail: matteo.angelinelli2@unibo.it
[2] INAF, Osservatorio di Astrofisica e Scienza dello Spazio, Via Pietro Gobetti 93/3, 40121 Bologna, Italy
[3] INFN, Sezione di Bologna, Viale Berti Pichat 6/2, 40127 Bologna, Italy
[4] Universitäts-Sternwarte, Fakultät für Physik, Ludwig-Maximilians-Universität München, Scheinerstr.1, 81679 München, Germany
[5] Max-Planck-Institut für Astrophysik, Karl-Schwarzschild-Straße 1, 85741 Garching, Germany
[6] Hamburger Sternwarte, University of Hamburg, Gojenbergsweg 112, 21029 Hamburg, Germany
[7] Istituto di Radio Astronomia, INAF, Via Gobetti 101, 40121 Bologna, Italy
[8] INAF, Osservatorio Astronomico di Trieste, Via G.B. Tiepolo 11, 34143 Trieste, Italy
[9] IFPU, Institute for Fundamental Physics of the Universe, Via Beirut 2, 34014 Trieste, Italy

Received 20 May 2022 / Accepted 23 June 2022

**ABSTRACT**

We study the distributions of the baryons in massive halos ($M_{\rm vir} > 10^{13}\,h^{-1}\,M_\odot$) in the Magneticum suite of smoothed particle hydrodynamical cosmological simulations, out to the unprecedented radial extent of $10R_{500,c}$. We confirm that, under the action of non-gravitational physical phenomena, the baryon mass fraction is lower in the inner regions ($<R_{500,c}$) of increasingly less massive halos, and rises moving outwards, with values that span from 51% (87%) of the cosmological value in the regions around $R_{500,c}$ to 95% (100%) at $10R_{500,c}$ in the systems with the lowest (highest; $M_{\rm vir} \sim 5\times10^{14}\,h^{-1}\,M_\odot$) masses. The galaxy groups almost match the gas (and baryon) fraction measured in the most massive halos only at very large radii ($r > 6R_{500,c}$), where the baryon depletion factor $Y_{\rm bar} = f_{\rm bar}/(\Omega_{\rm b}/\Omega_{\rm m})$ approaches the value of unity, expected for 'closed-box' systems. We find that both the radial and mass dependence of the baryon, gas, and hot depletion factors are predictable and follow a simple functional form. The star mass fraction is higher in less massive systems, decreases systematically with increasing radii, and reaches a constant value of $Y_{\rm star} \approx 0.09$, where the gas metallicity is also constant, regardless of the host halo mass, as a result of the early ($z > 2$) enrichment process.

**Key words.** methods: numerical – large-scale structure of Universe – galaxies: clusters: intracluster medium – galaxies: groups: general – hydrodynamics – galaxies: clusters: general

## 1. Introduction

Knowing the baryon content of groups and clusters of galaxies, the most massive gravitationally bound structures in the Universe, is key to connecting their evolution with cosmology. A general expectation is that the relative amount of baryons they contain, with respect to their total mass, must match the ratio between the cosmological baryon density, $\Omega_{\rm b}$, and the total matter density, $\Omega_{\rm m}$. However, for this to be true, sufficiently large volumes must be considered in order to treat such systems as 'closed boxes' (Gunn et al. 1972; Bertschinger 1985; Voit 2005) and allow the additional, time-integrated effect of feedback from galaxy formation to be neglected (e.g., Allen et al. 2011). Any departure from the ideal condition of a closed box should leave an imprint on the distribution of the different components of the baryon budget as a function of both radius and halo mass (Limber 1959). Galaxy groups with typical masses of $10^{13-14}\,M_\odot$, being characterised by a shallower gravitational potential than the one found in more massive systems, can hardly be considered as 'closed'. They are thus unique laboratories for studying the interplay of the many different physical processes that affect the evolution of baryonic matter during the hierarchical structure formation (Springel 2005), as well as the energetic feedback from the many galaxies that co-evolve within them (or are continuously accreted over time). The fact that the galaxy groups are at the peak of the halo mass function makes their cosmological and astrophysical role particularly relevant.

Many observational studies (Sun et al. 2009; Ettori 2015; Lovisari et al. 2015; Eckert et al. 2016; Nugent et al. 2020) show how the baryon fraction in the central region of galaxy clusters and groups ($<R_{500,c}$) increases with the mass of the system. In the external regions, the gas distribution is only slightly constrained by X-ray observations because of their low signal with respect to the local background, although they are physically more interesting because of the increased complexity of processes that regulate the status of the gas, including some expected residual amount of non-thermal pressure (e.g., Angelinelli et al. 2020). If the expectations for a self-similar formation scenario are met for the most massive systems, then, at the group scale, the baryon content is only half of that expected from the self-similar scenario (see e.g. the review by Eckert et al. 2021). While the low X-ray surface brightness hampers observational attempts to constrain the gas content of galaxy groups and clusters (though for the most massive systems, constraints

around $R_{200,c}$ are available in e.g., Ghirardini et al. 2019), numerical simulations are overall able to correctly reproduce many different observed physical proprieties of the gas enclosed in galaxy groups, even if the proprieties of galaxies are not well constrained (see e.g., Oppenheimer et al. 2021; Gastaldello et al. 2021). Galaxy groups are the environment where the physical mechanisms that occur on galactic scales become less dominant, though are still important, with respect to the gravity that rules on cluster scales. Large-scale numerical cosmological simulations are then needed to recover the physical properties of these elusive and numerous systems (Ettori et al. 2006; Planelles et al. 2013; Haider et al. 2016; McCarthy et al. 2017; Pillepich et al. 2018; Biffi et al. 2018c; Vallés-Pérez et al. 2020; Galárraga-Espinosa et al. 2022, and references therein), as well as to facilitate realistic predictions for the next generation of X-ray observatories (Roncarelli et al. 2018).

In this work we perform a dedicated analysis of baryon and gas fractions in regions in the outskirts of galaxy clusters and beyond in a sample of halos simulated by the Magneticum[1] suite. This work is structured as follows: in Sect. 2 we briefly describe the Magneticum simulations and our sample; in Sect. 3 we present the results of our analysis and a comparison with recent observational and numerical constraints. In Sect. 5 we discuss our main findings, the limitations of our analysis, and possible implications for future work.

## 2. Cosmological simulations: Magneticum

We selected a sub-sample of galaxy clusters and groups, part of the simulated *Box2b/hr* of Magneticum simulations at redshift $z = 0.25$, the last available snapshot for this simulated box. The high resolution run of *Box2b* includes a total of $2 \cdot 2880^3$ particles in a volume of $(640\,h^{-1}\,\mathrm{cMpc})^3$. The particle masses are $6.9 \times 10^8\,h^{-1}\,M_\odot$ and $1.4 \times 10^8\,h^{-1}\,M_\odot$, respectively, for dark matter and the gas component, and the stellar particles have a softening of $\epsilon = 2\,h^{-1}$ ckpc. The cosmology adopted for these simulations is the WMAP7 from Komatsu et al. (2011), with a total matter density of $\Omega_\mathrm{m} = 0.272$, of which 16.8% is baryons, the cosmological constant $\Lambda_0 = 0.728$, the Hubble constant $H_0 = 70.4\,\mathrm{km\,s^{-1}\,Mpc^{-1}}$, the index of the primordial power spectrum $n = 0.963$, and the overall normalisation of the power spectrum $\sigma_8 = 0.809$. The more relevant physical mechanisms included in Magneticum are: cooling, star formation, and winds with velocities of $350\,\mathrm{km\,s^{-1}}$ (Springel & Hernquist 2002); an explicit tracing of metal species (namely, C, Ca, O, N, Ne, Mg, S, Si, and Fe), a detailed tracking of the stellar population and chemical enrichment by Type Ia supernovae (SN-Ia), Type II supernovae (SN-II), and asymptotic giant branch (AGB) stars (Tornatore et al. 2003, 2007) and cooling tables from Wiersma et al. (2009); black holes and associated active galactic nucleus (AGN) feedback (Springel et al. 2005) with various improvements (Fabjan et al. 2010; Hirschmann et al. 2014) for the treatment of the black hole sink particles and the different feedback modes; isotropic thermal conduction of 1/20 of the standard *Spitzer* value (Dolag et al. 2004); a low viscosity scheme to track turbulence (Dolag et al. 2005b; Beck et al. 2016); higher-order smoothed particle hydrodynamic kernels (Dehnen & Aly 2012); and passive magnetic fields (Dolag & Stasyszyn 2009). Halos are identified using SUBFIND (Springel et al. 2001; Dolag et al. 2009), where the centre of a halo is defined as the position of the particle with the minimum of the gravitational potential. The virial mass, $M_\mathrm{vir}$, is defined through the spherical overdensity as predicted by the generalised spherical top-hat collapse model (Eke et al. 1996). In particular, it is referred to $R_\mathrm{vir}$, whose overdensity to the critical density follows Eq. (6) of Bryan & Norman (1998), which corresponds to ≈117 for the given redshift and cosmology. The radius $R_{200,m}$ (respectively $R_{500,c}$) is defined as a spherical overdensity of 200 (respectively 500) to the mean (respectively critical) density in the chosen cosmology.

As shown in previous studies, the galaxy physics implemented in the Magneticum simulations leads to a successful reproduction of basic galaxy properties, such as the stellar mass function (Naab & Ostriker 2017; Lustig et al. 2022), the environmental impact of galaxy clusters on galaxy properties (Lotz et al. 2019), and the appearance of post-starburst galaxies (Lotz et al. 2021), as well as the associated AGN population at various redshifts (Hirschmann et al. 2014; Steinborn et al. 2016; Biffi et al. 2018a). At the cluster scale, Magneticum simulations have demonstrated its ability to reproduce the observable X-ray luminosity relation (Biffi et al. 2013), the pressure profile of the intracluster medium (ICM) (Gupta et al. 2017), the chemical composition of the ICM (Dolag et al. 2017; Biffi et al. 2018b), the high concentration observed in fossil groups (Ragagnin et al. 2019), and the gas properties in between galaxy clusters (Biffi et al. 2022). On larger scales, Magneticum simulations have been able to reproduce the observed Sunyaev–Zeldovich (SZ) power spectrum (Dolag et al. 2016) as well as the observed thermal history of the Universe (Young et al. 2021).

To build our sample, we divided the mass range between $M_\mathrm{vir}$ values of $10^{13}\,h^{-1}\,M_\odot$ and $>5 \times 10^{14}\,h^{-1}\,M_\odot$ (corresponding to $M_{500,c}$ between $4.2{\times}10^{12}\,h^{-1}\,M_\odot$ and $5.4{\times}10^{14}\,h^{-1}\,M_\odot$ for the less massive and the most massive system, respectively) into 14 equal bins in logarithmic space. For each bin, we randomly selected ten objects from the simulated *Box2b*. The final sample is composed of a total of 140 galaxy groups and clusters, where the smallest halo is represented by $4.6{\times}10^4$ particles in the radial range shown in Fig. 1, which gives the density profiles for each object as well as the median values computed in the 14 mass bins.

In addition, Fig. 1 also shows two gas density maps for the most massive and least massive objects in our sample, produced using the software SMAC (Dolag et al. 2005a). To also have an upper limit for the radial range of our analysis, we considered the position of the accretion shocks to be the boundary of our system. Different definitions of the position of accretion shocks can be found in the literature (Zhang et al. 2020; Aung et al. 2021). In our work, we assumed the position of the accretion shocks to be located at the same radius at which the gas entropy profile reaches its peak (Vazza et al. 2011). Expressing this distance as a function of $R_{200,m}$, we find that the median distance of the accretion shock from the system centre is $3(\pm1)R_{200,m}$. Moreover, for our sample, we find also that $R_{200,m}$ is $2.3(\pm0.1)R_{500,c}$. As we wanted to characterise the baryon and gas fractions inside the entire volume of our galaxy groups and clusters, we combined these values and extended our analysis up to $10R_{500,c}$. A more detailed study of the position of accretion shocks in our sample will be part of a forthcoming paper.

## 3. The gas and baryon fractions out to $10R_{500,c}$

We defined the baryon, gas, and star fractions as

$$f_\mathrm{bar}(<r) = (m_\mathrm{gas}(<r) + m_\mathrm{star}(<r) + m_\mathrm{BH}(<r))/m_\mathrm{tot}(<r) \quad (1)$$

$$f_\mathrm{gas}(<r) = m_\mathrm{gas}(<r)/m_\mathrm{tot}(<r) \quad (2)$$

$$f_\mathrm{star}(<r) = m_\mathrm{star}(<r)/m_\mathrm{tot}(<r), \quad (3)$$

[1] http://www.magneticum.org

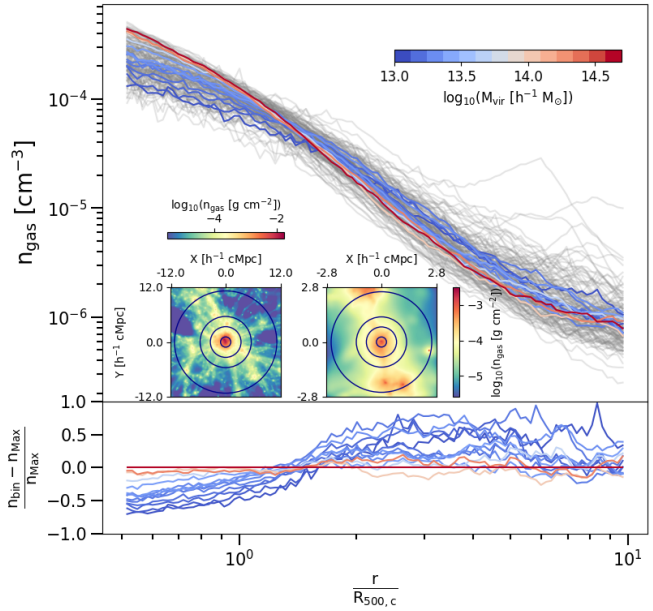


**Fig. 1.** Gas density profiles and maps. *Top*: radial profiles of gas density from $0.5R_{500,c}$ up to $10R_{500,c}$. Grey lines indicate profiles of single objects, while coloured lines are the median values computed in different mass bins (see the colour legend). *Bottom*: median radial profiles of the gas density of different mass bins computed with respect to the median radial profile of the most massive bin (same colour legend as the upper plot). Insets: projected 2D electron gas density maps for the most massive (*left*; $M_{vir} = 9.8 \times 10^{14}\,h^{-1}\,M_\odot$, $R_{500,c} = 1120.4\,h^{-1}$ ckpc) and the least massive (*right*; $M_{vir} = 10^{13}\,h^{-1}\,M_\odot$, $R_{500,c} = 252.5\,h^{-1}$ ckpc) objects in our sample. The blue circles represent 1, 3, 5, and $10R_{500,c}$.

where $r$ is the radial distance from the cluster or group centre. The different $m_i(<r)$ are referred to different particle types (gas, stars, or black holes), while $m_{\rm tot}(<r)$ is the sum of the previous masses and the dark matter up to the radial shell, $r$. Regarding the black holes, which are no longer considered in our analysis, their median mass is $7 \times 10^8\,h^{-1}\,M_\odot$ and their contribution to the total baryon budget rapidly decreases at greater radial distances from the centre of the system, from 0.2% to 0.02%, without strong dependences on the halo mass. In the following we use the depletion parameter $Y$, defined as

$$Y(<r) = f(<r)/(\Omega_{\rm b}/\Omega_{\rm m}), \tag{4}$$

where $f(<r)$ could assume any definition given above and $\Omega_{\rm b}/\Omega_{\rm m} = 0.168$, the cosmological value of baryon over the total matter adopted for Magneticum simulations.

Firstly, we compared our results with the numerical and observational literature. In particular, in the left panel of Fig. 2, we compare our gas depletion with the values reported by Kravtsov et al. (2005) and Planelles et al. (2013). We can conclude from this comparison that the gas depletion factor we recover at $R_{500,c}$ for the most massive systems is in line with the numerical literature. However, on group mass scales, we expect the potential well to be less effective in bounding the accreting baryons and balancing the dispersive actions of feedback from AGN and winds from star-formation activity. Therefore, we expect a decrease in the gas depletion factor moving towards lower mass scales (see e.g., Eckert et al. 2021; Akino et al. 2022). In Fig. 2 we show how our simulated dataset is able to recover the expected and observed behaviour within $R_{500,c}$.

In Fig. 3 we show the distributions of the baryon ($Y_{\rm bar}$), gas ($Y_{\rm gas}$), and star ($Y_{\rm star}$) depletion factors as functions of the radius (between $0.5R_{500,c}$ and $10R_{500,c}$) and halo mass. We show that, although the baryon fraction is always ≥50% of the cosmological value $\Omega_{\rm b}/\Omega_{\rm m}$ in each mass bin, it reaches the cosmological value only at radii larger than $5R_{500,c}$ and only in the most massive systems. Indeed, $Y_{\rm bar}$ is greater than 0.99 at $r > 5R_{500,c}$ in sub-sample D (comprising the most massive systems in our catalogue), whereas it has a value of about 0.83 at $5R_{500,c}$ and 0.95 at $10R_{500,c}$ (see Table A.1). Similar trends are observed for the gas depletion factor, $Y_{\rm gas}$. Also in this case, the larger the radii, the higher the depletion factor. Both for the baryonic matter and for the hot gas alone, less massive systems show a steeper increase in the depletion factor with increasing radius. On the contrary, the stellar depletion factor, $Y_{\rm star}$, decreases with the radius and is higher in less massive systems. At larger radii, this behaviour is less prominent and both galaxy groups and clusters show constant and similar values of $Y_{\rm star} = 0.09^{+0.01}_{-0.01}$, confirming that the in situ enrichment does not play a significant role and that its uniform metal abundance is rather the consequence of the accretion of pre-enriched (at $z > 2$) gas (see Biffi et al. 2018c). On the other hand, a more efficient production of stars is required by the larger $Y_{\rm star}$ estimated in less massive halos within $R_{500,c}$.

Focusing on the gas component of our systems, we define $f_{\rm hot}$ and $f_{\rm cold}$:

$$f_{\rm hot}(<r) = m_{\rm hot}(<r)/m_{\rm tot}(<r) \tag{5}$$
$$f_{\rm cold}(<r) = m_{\rm cold}(<r)/m_{\rm tot}(<r), \tag{6}$$

meaning a selection of gas particles based on the temperature, 'hot' for particles with temperatures greater than 0.1 keV and 'cold' for the others. In the right panel of Fig. 3, we show the radial behaviour of these quantities compared to $Y_{\rm gas}$. We note that the cold component of gas content became important at very large radii, over $6R_{500,c}$. Moreover, this cold component shows larger values for galaxy groups: it is larger than 0.2 at radii greater than $8R_{500,c}$. The hot phase presents a drop for all the mass bins at radii larger than $6R_{500,c}$, where we locate the accretion shocks in our systems on average (see Sect. 2). This means that, at the larger radii we investigate, there are also contributions from the environment in which galaxy groups and clusters reside, with a decreasing contribution to the expected gas emissivity in X-rays.

## 4. The radial trend of gas metallicity

The injection and evolution of metals by SN-Ia, SN-II, and AGB stars in Magneticum simulations are modelled following Tornatore et al. (2003, 2007). Although the simulation traces various elements individually, we consider here the total metallicity, that is to say, the sum of the elements heavier than helium relative to the hydrogen mass. Then, the total metallicity at each radial shell, $r$, $Z_{\rm tot}(r)$, is the mass-weighted sum of the metallicity of the gas particles, $i$, with mass $m_{\rm gas,i}$ that belong to the radial shell, $r$:

$$Z_{\rm tot}(r) = \frac{\sum_i Z_{{\rm tot},i} \cdot m_{{\rm gas},i}}{\sum_i m_{{\rm gas},i}}. \tag{7}$$

The radial shells are defined to include a fixed number of 250 particles to allow a significant statistical analysis of each of them. We normalised these values of metallicity to the solar values proposed by Asplund et al. (2009): $Z_\odot = 0.0142$.

In Fig. 4 we show the metallicity profiles recovered up to $10R_{500,c}$ in all our halos. The profiles are remarkably similar, flattening to a constant value of about $0.23^{+0.08}_{-0.08}$ at $r > 2R_{500,c}$

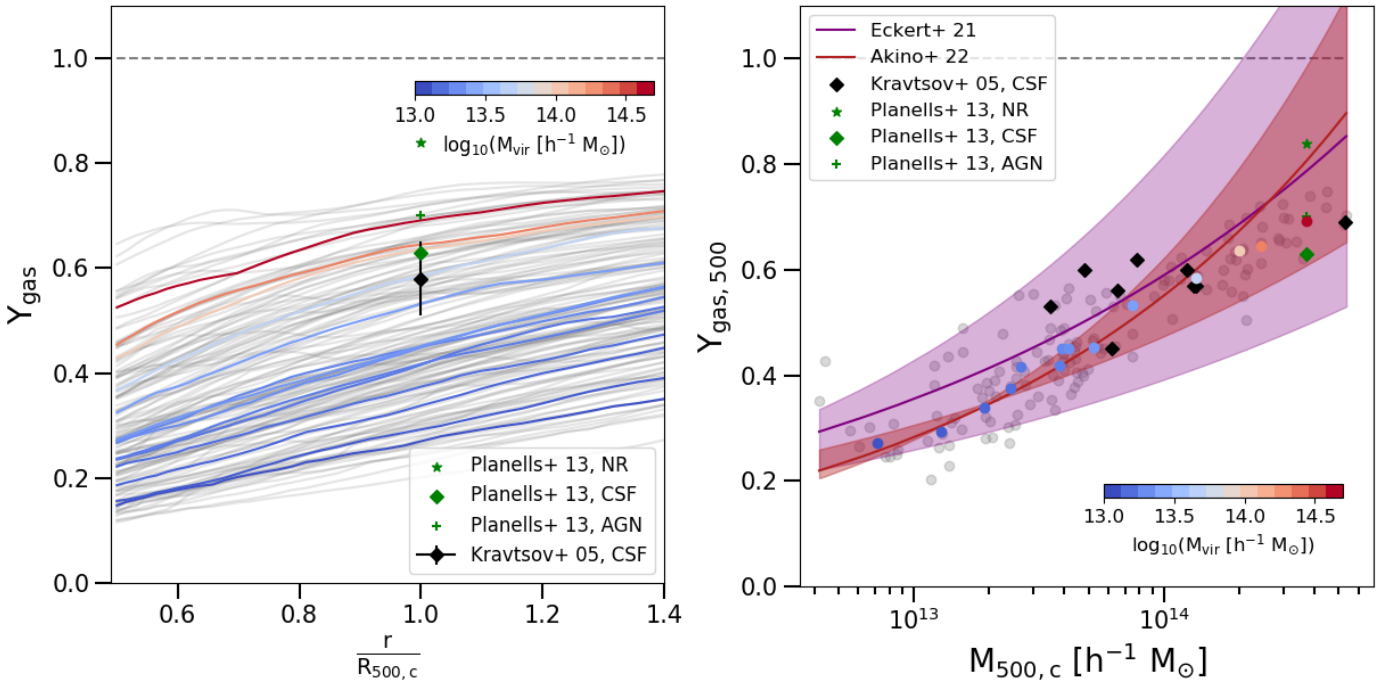


**Fig. 2.** Gas depletion in our sample compared with previous works. *Left*: radial profiles of gas depletion, from $0.5R_{500,c}$ up to $1.4R_{500,c}$. Grey lines represent single objects in our sample, while the coloured ones are the median values computed in mass bins. Comparison numerical estimates from the literature are given by different symbols (black, Kravtsov et al. 2005; green, Planelles et al. 2013). From Kravtsov et al. (2005), we consider the mean value and its scatter for $Y_{\rm gas}$ at $R_{500,c}$ in the simulations with gas dynamics and several physical processes (CSF). From Planelles et al. (2013), we plot the non-radiative run (NR), the run with star formation and feedback from a supernova explosion (CSF), and a run with the additional contribution from AGN (AGN). *Right*: gas depletion parameter at $R_{500,c}$ as a function of $M_{500,c}$. Grey dots represent single objects in our sample, while the coloured ones are the median values computed in mass bins. The constraints from Kravtsov et al. (2005) (black points) are indicated in correspondence with the mass of single clusters in their analysis, whereas for Planelles et al. (2013) (green points) they are indicated in correspondence with our most massive bin. The lines and related shadow regions are the best fits proposed by Eckert et al. (2021) (purple; $f_{\rm gas,500} = 0.079^{+0.026}_{-0.025}(M_{500}/10^{14}\,M_\odot)^{0.22^{+0.06}_{-0.04}}$) and Akino et al. (2022) (brick red; $ln(M_{\rm gas}/10^{12}\,M_\odot) = 1.95^{+0.08}_{-0.08} + 1.29^{+0.16}_{-0.10}\ln(M_{500}/10^{14}\,M_\odot)$).

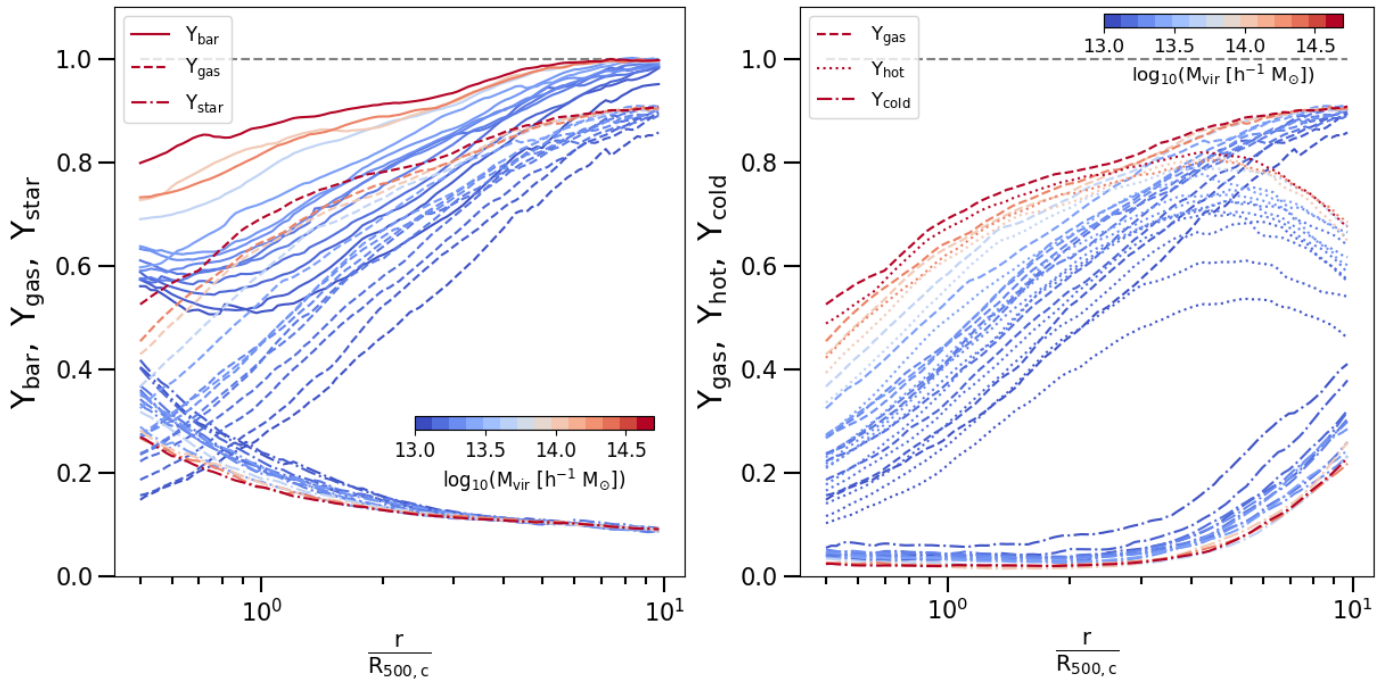


**Fig. 3.** Depletion factors in our sample. *Left*: radial profiles of baryon, gas, and star depletion, from $0.5R_{500,c}$ up to $10R_{500,c}$. The lines represent the median profiles in each mass bin, while the different line styles represent baryon (solid), gas (dashed), or star depletion (dash-dotted). *Right*: same as the plot on the left, but representing only three different gas particle selections: gas particles (dashed), hot gas with temperatures greater than 0.1 keV (dotted), and cold gas with temperatures below 0.1 keV (dash-dotted).

and with a negligible dependence on the halo mass (see the median estimates in Table A.1). Some mass dependence would be expected as a consequence of any difference in star-formation activities from group to cluster scales, because groups are less effective in producing and releasing metals into their environment. The lack of evidence of such a dependence supports the expectations of the early enrichment scenario. Biffi et al. (2017; see also Biffi et al. 2018c) find that at $r > 0.2R_{180}$ the metallicity is remarkably homogeneous, with almost flat profiles of the elements produced by either SN-Ia or SN-II, mostly as a consequence of the widespread displacement of metal-rich gas by early, powerful AGN bursts ($z > 2-3$) acting on small high-redshift halos, and with no significant evolution since redshift ∼2.

Given the large scatter observed in single radial profiles of metallicity in Fig. 4, we investigated the relations between the masses of the systems and metallicity. From the left panel of Fig. 5, where we show the metallicity as a function of gas mass, we note how the profiles are still highly scattered. However, looking at the values of metallicity computed at $R_{500,c}$ (the coloured dots in the plot), we also notice that galaxy groups (bluish dots) show a higher spread in metallicity than the galaxy clusters (reddish dots), with median values of $0.29^{+0.11}_{-0.11}$ and $0.30^{+0.06}_{-0.07}$, respectively. This trend is similar to the findings discussed by Truong et al. (2019), who focused on the iron contribution in extremely central regions of simulated galaxy clusters and groups ($r < 0.1R_{500}$). They also compared their results with observational work by Mernier et al. (2018). On the other hand, in the central and right panels of Fig. 5, we present the density-temperature phase diagram for the least (centre) and most (right) massive objects in our sample, colour-coding by the mass-weighted metallicity of each density-temperature bin. Here, we notice a high spread of metallicity values for both galaxy groups and clusters. Even when we consider the hot and cold gas phases separately, the scatter in metallicity is still present. From Fig. 5 as a whole, we conclude that the observed scatter in radial profiles of metallicity is due to an intrinsic scatter present in the gas particles. Moreover, the coexistence of different gas phases tends to enlarge the observed scatter.

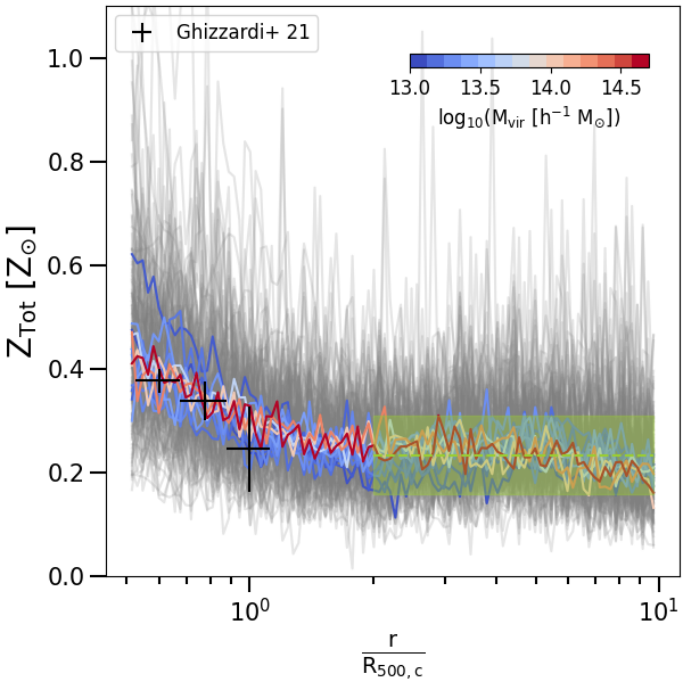


**Fig. 4.** Radial profiles of gas metallicity from $0.5R_{500,c}$ up to $10R_{500,c}$. Grey lines represent single objects, while the coloured ones are the mean values computed in mass bins. The dashed green line and its related shadow region show the median and the 16th and 84th percentiles of the gas metallicity distribution over $2R_{500,c}$ ($0.23^{+0.08}_{-0.08}$). The black dots are the observed estimates of gas metallicity from Ghizzardi et al. (2021).

## 5. Discussion and conclusions

While galaxy clusters, in particular the most massive and relaxed ones, are direct proxies of the cosmological baryon fraction (e.g., Allen et al. 2008; Ettori et al. 2009; Mantz et al. 2022), galaxy groups host an environment where the competing effects of gravity and the stellar and AGN feedbacks break the self-similar expectations regarding the gas distribution. Realistic numerical simulations are thus key to producing accurate 3D models of the likely distribution of gas in and around halos as a function of their mass.

We considered a large sample of 140 galaxy groups and clusters with $M_{\rm vir} > 10^{13}\,h^{-1}\,M_\odot$ at $z = 0.25$, simulated at high resolution with the Magneticum runs and analysed up to $10R_{500,c}$ (i.e., roughly beyond the location of the accretion shock). We focused our analysis on the radial dependence of the depletion factors $Y_{\rm bar}$, $Y_{\rm gas}$, and $Y_{\rm star}$ (see the definitions in Sect. 3), well beyond the currently available constraints at $\sim R_{200,c}$. We summarise here our main results:

– We verified that the baryon fraction is always >50% of the cosmological value adopted in our simulations at $r > R_{500,c}$ and at any mass bin. It reaches that value at $\sim 5R_{500,c}$, but only in the most massive systems. The $Y_{\rm bar}$ in less massive systems, though it shows steeper radial profiles, remains 5% below $\Omega_{\rm b}/\Omega_{\rm m}$, even at $10R_{500,c}$ (see Fig. 3 and Table A.1). Similar trends are observed for the gas component.
– Once we divided the gas component into two different phases, hot when the temperature of the particle is greater than 0.1 keV and cold for the remaining gas, the contribution given by the cold phase is quite negligible inside $6R_{500,c}$, whereas beyond this limit, especially for less massive objects, it gradually becomes more important, reaching 45% of the entire gas contribution for galaxy groups and 25% for galaxy clusters at $10R_{500,c}$ (see Fig. 3). The hot, X-ray-detectable phase is a good tracer of the total amount of gas at all the masses and always represents more than 90% (70%) of it in the most (least) massive objects within $5R_{500,c}$. At about $6R_{500,c}$, $Y_{\rm hot}$ shows a drop for all mass bins. This drop is consistent with the position of the accretion shock.
– We find that both the radial and mass dependences of $Y_{\rm bar}$, $Y_{\rm gas}$, and $Y_{\rm hot}$ (see Fig. 3) are predictable and follow the following functional form:

$$Y_i = \alpha \cdot w^{\beta} \cdot x^{\gamma + \delta * w}, \tag{8}$$

where $w = M_{500,c}/5 \times 10^{14}\,h^{-1}\,M_\odot$, $x = r/R_{500,c}$, and $\alpha, \beta, \gamma$, and $\delta$ are the free parameters quoted in Table A.2. The set of parameters $(\alpha, \beta, \gamma, \delta) = (0.90, 0.12, 0.23, -0.22)$ provides a description within 2% of $Y_{\rm bar}$ (see Fig. A.1).
– The $Y_{\rm star}$ decreases systematically with increasing radii. While the contribution of the stellar mass fraction in the central region ($<2R_{500,c}$) is higher in less massive systems, this difference disappears at larger radii, and both galaxy groups and clusters reach a value of $Y_{\rm star} = 0.09^{+0.01}_{-0.01}$. In these regions, the metal distribution becomes constant, with a median value of $0.23^{+0.08}_{-0.08}$ at $r > 2R_{500,c}$, with no dependence

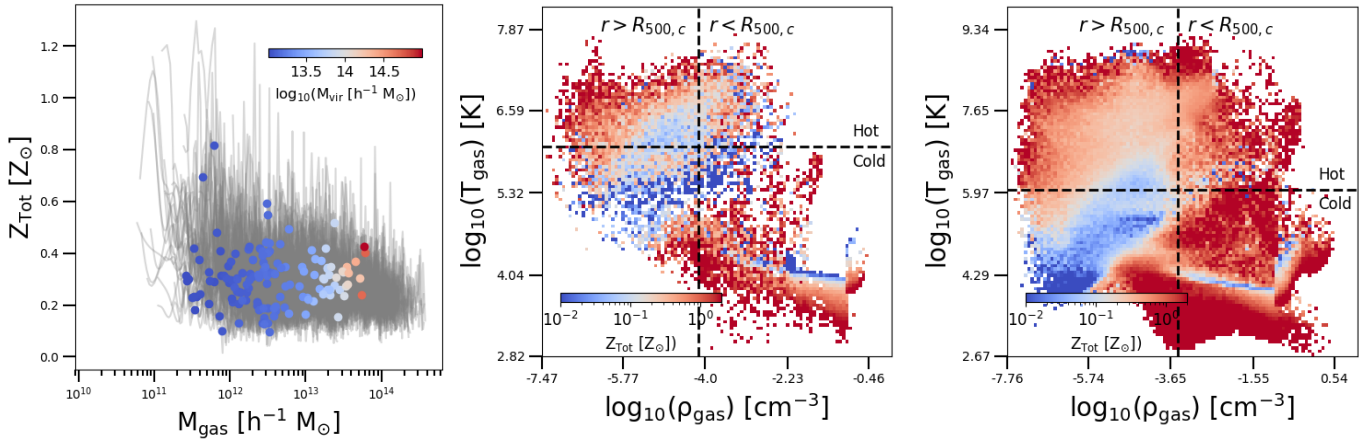


**Fig. 5.** Metallicity as a function of mass and phase diagrams. *Left*: metallicity as a function of gas mass. The grey lines represent the profiles computed for single objects in our sample, whereas the coloured dots are the values computed at $R_{500,c}$ (again, for each group and cluster present in our sample). The colour-coding is given by the virial mass ($M_{\rm vir}$) of the systems. *Centre and right*: density–temperature phase diagram for the less massive system (*centre*; $M_{\rm vir} = 10^{13}\,h^{-1}\,M_{\odot}$) and the most massive one in our sample (*right*; $M_{vir} = 9.8 \times 10^{14}\,h^{-1}\,M_{\odot}$). The colour-coding is given by the mass-weighted metallicity in each density–temperature bin. The dashed horizontal black lines represent the 0.1 keV ($1.16 \times 10^6$ K) temperature cut, adopted to separate 'hot' and 'cold' gas phases. The dashed vertical line marks the gas density at $R_{500,c}$. To the right of this line are the particles inside $R_{500,c}$, and to the left the particles located at larger radii.

on the halo mass (see Fig. 4 and Table A.1). These flat mass-independent metallicity profiles support a scenario in which the gas present in massive halos is enriched early, with a negligible contribution from recent star-formation processes (i.e., the gas is indeed expected to be mass-dependent). This result confirms, and extends to much larger radii, what has been obtained from recent work on numerical simulations (see e.g., Biffi et al. 2017, 2018c).

This study has explored the properties of the baryons in massive halos ($M_{\rm vir} > 10^{13}\,h^{-1}\,M_{\odot}$) well outside the virialised regions, where material from the cosmic field is still accreted. We have convincingly shown that these halos converge in a different way (depending on their mass) to common properties in terms of baryon, gas, stellar, and metal distribution as they approach the mean location of the accretion shock ($\sim 6R_{500,c}$). This work allows us to make firm predictions on the average distribution of the baryons in their different phases in regions with both current ($r < R_{500,c}$) and possible future observational constraints, indicating, for instance, where to look for gas that is not (X-ray) detected on the mass scales of the galaxy groups.

*Acknowledgements.* S.E. acknowledges financial contribution from the contracts ASI-INAF Athena 2019-27-HH.0, "Attività di Studio per la comunità scientifica di Astrofisica delle Alte Energie e Fisica Astroparticellare" (Accordo Attuativo ASI-INAF n. 2017-14-H.0), INAF mainstream project 1.05.01.86.10, and from the European Union's Horizon 2020 Programme under the AHEAD2020 project (grant agreement n. 871158). M.A. and F.V. acknowledge the financial support by the H2020 initiative, through the ERC StG MAGCOW (n. 714196). A.R. acknowledges support from the grant PRIN-MIUR 2017 WSCC32. KD acknowledges supported by the Excellence Cluster ORIGINS which is funded by the Deutsche Forschungsgemeinschaft (DFG, German Research Foundation) under Germany's Excellence Strategy – EXC-2094 – 390783311 and funding for the COMPLEX project from the European Research Council (ERC) under the European Union's Horizon 2020 research and innovation program grant agreement ERC-2019-AdG 882679. The calculations for the hydro-dynamical simulations were carried out at the Leibniz Supercomputer Center (LRZ) under the project pr83li. We are especially grateful for the support by M. Petkova through the Computational Center for Particle and Astrophysics (C2PAP).

## References

Akino, D., Eckert, D., Okabe, N., et al. 2022, PASJ, 74, 175
Allen, S. W., Rapetti, D. A., Schmidt, R. W., et al. 2008, MNRAS, 383, 879
Allen, S. W., Evrard, A. E., & Mantz, A. B. 2011, ARA&A, 49, 409
Angelinelli, M., Vazza, F., Giocoli, C., et al. 2020, MNRAS, 495, 864
Asplund, M., Grevesse, N., Sauval, A. J., & Scott, P. 2009, ARA&A, 47, 481
Aung, H., Nagai, D., & Lau, E. T. 2021, MNRAS, 508, 2071
Beck, A. M., Murante, G., Arth, A., et al. 2016, MNRAS, 455, 2110
Bertschinger, E. 1985, ApJS, 58, 39
Biffi, V., Dolag, K., & Böhringer, H. 2013, MNRAS, 428, 1395
Biffi, V., Planelles, S., Borgani, S., et al. 2017, MNRAS, 468, 531
Biffi, V., Dolag, K., & Merloni, A. 2018a, MNRAS, 481, 2213
Biffi, V., Mernier, F., & Medvedev, P. 2018b, Space Sci. Rev., 214, 123
Biffi, V., Planelles, S., Borgani, S., et al. 2018c, MNRAS, 476, 2689
Biffi, V., Dolag, K., Reiprich, T. H., et al. 2022, A&A, 661, A17
Bryan, G. L., & Norman, M. L. 1998, ApJ, 495, 80
Dehnen, W., & Aly, H. 2012, MNRAS, 425, 1068
Dolag, K., & Stasyszyn, F. 2009, MNRAS, 398, 1678
Dolag, K., Jubelgas, M., Springel, V., Borgani, S., & Rasia, E. 2004, ApJ, 606, L97
Dolag, K., Hansen, F. K., Roncarelli, M., & Moscardini, L. 2005a, MNRAS, 363, 29
Dolag, K., Vazza, F., Brunetti, G., & Tormen, G. 2005b, MNRAS, 364, 753
Dolag, K., Borgani, S., Murante, G., & Springel, V. 2009, MNRAS, 399, 497
Dolag, K., Komatsu, E., & Sunyaev, R. 2016, MNRAS, 463, 1797
Dolag, K., Mevius, E., & Remus, R.-S. 2017, Galaxies, 5, 35
Eckert, D., Ettori, S., Coupon, J., et al. 2016, A&A, 592, A12
Eckert, D., Gaspari, M., Gastaldello, F., Le Brun, A. M. C., & O'Sullivan, E. 2021, Universe, 7, 142
Eke, V. R., Cole, S., & Frenk, C. S. 1996, MNRAS, 282, 263
Ettori, S. 2015, MNRAS, 446, 2629
Ettori, S., Dolag, K., Borgani, S., & Murante, G. 2006, MNRAS, 365, 1021
Ettori, S., Morandi, A., Tozzi, P., et al. 2009, A&A, 501, 61
Fabjan, D., Borgani, S., Tornatore, L., et al. 2010, MNRAS, 401, 1670
Galárraga-Espinosa, D., Langer, M., & Aghanim, N. 2022, A&A, 661, A115
Gastaldello, F., Simionescu, A., Mernier, F., et al. 2021, Universe, 7, 208
Ghirardini, V., Eckert, D., Ettori, S., et al. 2019, A&A, 621, A41
Ghizzardi, S., Molendi, S., van der Burg, R., et al. 2021, A&A, 646, A92
Gunn, J. E., Gott, J., & Richard, I. 1972, ApJ, 176, 1
Gupta, N., Saro, A., Mohr, J. J., Dolag, K., & Liu, J. 2017, MNRAS, 469, 3069
Haider, M., Steinhauser, D., Vogelsberger, M., et al. 2016, MNRAS, 457, 3024
Hirschmann, M., Dolag, K., Saro, A., et al. 2014, MNRAS, 442, 2304
Komatsu, E., Smith, K. M., Dunkley, J., et al. 2011, ApJS, 192, 18
Kravtsov, A. V., Nagai, D., & Vikhlinin, A. A. 2005, ApJ, 625, 588
Limber, D. N. 1959, ApJ, 130, 414
Lotz, M., Remus, R.-S., Dolag, K., Biviano, A., & Burkert, A. 2019, MNRAS, 488, 5370
Lotz, M., Dolag, K., Remus, R.-S., & Burkert, A. 2021, MNRAS, 506, 4516
Lovisari, L., Reiprich, T. H., & Schellenberger, G. 2015, A&A, 573, A118
Lustig, P., Strazzullo, V., Remus, R. S., et al. 2022, MNRAS, submitted [arXiv:2201.09068]

Mantz, A. B., Morris, R. G., Allen, S. W., et al. 2022, MNRAS, 510, 131
McCarthy, I. G., Schaye, J., Bird, S., & Le Brun, A. M. C. 2017, MNRAS, 465, 2936
Mernier, F., de Plaa, J., Werner, N., et al. 2018, MNRAS, 478, L116
Naab, T., & Ostriker, J. P. 2017, ARA&A, 55, 59
Nugent, J. M., Dai, X., & Sun, M. 2020, ApJ, 899, 160
Oppenheimer, B. D., Babul, A., Bahé, Y., Butsky, I. S., & McCarthy, I. G. 2021, Universe, 7, 209
Pillepich, A., Nelson, D., Hernquist, L., et al. 2018, MNRAS, 475, 648
Planelles, S., Borgani, S., Dolag, K., et al. 2013, MNRAS, 431, 1487
Ragagnin, A., Dolag, K., Moscardini, L., Biviano, A., & D'Onofrio, M. 2019, MNRAS, 486, 4001
Roncarelli, M., Gaspari, M., Ettori, S., et al. 2018, A&A, 618, A39
Springel, V. 2005, MNRAS, 364, 1105
Springel, V., & Hernquist, L. 2002, MNRAS, 333, 649
Springel, V., White, S. D. M., Tormen, G., & Kauffmann, G. 2001, MNRAS, 328, 726
Springel, V., Di Matteo, T., & Hernquist, L. 2005, MNRAS, 361, 776
Steinborn, L. K., Dolag, K., Comerford, J. M., et al. 2016, MNRAS, 458, 1013
Sun, M., Voit, G. M., Donahue, M., et al. 2009, ApJ, 693, 1142
Tornatore, L., Borgani, S., Springel, V., et al. 2003, MNRAS, 342, 1025
Tornatore, L., Borgani, S., Dolag, K., & Matteucci, F. 2007, MNRAS, 382, 1050
Truong, N., Rasia, E., Biffi, V., et al. 2019, MNRAS, 484, 2896
Vallés-Pérez, D., Planelles, S., & Quilis, V. 2020, MNRAS, 499, 2303
Vazza, F., Dolag, K., Ryu, D., et al. 2011, MNRAS, 418, 960
Voit, G. M. 2005, Rev. Mod. Phys., 77, 207
Wiersma, R. P. C., Schaye, J., Theuns, T., Dalla Vecchia, C., & Tornatore, L. 2009, MNRAS, 399, 574
Young, S., Komatsu, E., & Dolag, K. 2021, Phys. Rev. D, 104
Zhang, C., Churazov, E., Dolag, K., Forman, W. R., & Zhuravleva, I. 2020, MNRAS, 494, 4539

## Appendix A: Estimates and fitting parameters of the depletion factors

**Table A.1.** Baryons ($Y_{\rm bar}$), gas ($Y_{\rm gas}$), hot gas phase ($Y_{\rm hot}$), cold gas phase ($Y_{\rm cold}$), stellar depletion factors ($Y_{\rm star}$), and gas metallicity ($Z_{tot}$) computed at four different radii ($1, 3, 5$, and $10$ times $R_{500,c}$) for four virial mass bins ($A: 10^{13} < M_{vir}/h^{-1}M_\odot < 2\cdot10^{13}$ ($4.2\cdot10^{12} < M_{500,c}/h^{-1}M_\odot < 1.2\cdot10^{13}$); $B: 5\cdot10^{13} < M_{vir}/h^{-1}M_\odot < 6\cdot10^{13}$ ($1.6\cdot10^{13} < M_{500,c}/h^{-1}M_\odot < 3.6\cdot10^{13}$); $C: 10^{14} < M_{vir}/h^{-1}M_\odot < 2\cdot10^{14}$ ($6.3\cdot10^{13} < M_{500,c}/h^{-1}M_\odot < 10^{14}$); $D: M_{vir}/h^{-1}M_\odot > 5\cdot10^{14}$ ($M_{500,c}/h^{-1}M_\odot > 2.4\cdot10^{14}$)). Errors are given as 16th and 84th distribution percentiles. Note that the depletion factors are computed within the given radii, unlike the metallicity values, which are given within a spherical shell (considering the same reference radii).

| | | $R_{500,c}$ | $3R_{500,c}$ | $5R_{500,c}$ | $10R_{500,c}$ |
|---|---|---|---|---|---|
| A | $Y_{\rm bar}$ | $0.51^{+0.09}_{-0.06}$ | $0.70^{+0.06}_{-0.05}$ | $0.83^{+0.05}_{-0.01}$ | $0.95^{+0.04}_{-0.02}$ |
| | $Y_{\rm gas}$ | $0.27^{+0.06}_{-0.03}$ | $0.57^{+0.05}_{-0.03}$ | $0.73^{+0.05}_{-0.03}$ | $0.86^{+0.05}_{-0.03}$ |
| | $Y_{\rm hot}$ | $0.22^{+0.03}_{-0.02}$ | $0.48^{+0.05}_{-0.07}$ | $0.53^{+0.06}_{-0.08}$ | $0.46^{+0.14}_{-0.10}$ |
| | $Y_{\rm cold}$ | $0.06^{+0.03}_{-0.02}$ | $0.10^{+0.01}_{-0.02}$ | $0.21^{+0.04}_{-0.06}$ | $0.41^{+0.08}_{-0.10}$ |
| | $Y_{\rm star}$ | $0.24^{+0.03}_{-0.03}$ | $0.12^{+0.01}_{-0.01}$ | $0.11^{+0.01}_{-0.01}$ | $0.09^{+0.01}_{-0.01}$ |
| | $Z_{\rm tot}$ | $0.24^{+0.07}_{-0.02}$ | $0.17^{+0.05}_{-0.06}$ | $0.21^{+0.21}_{-0.05}$ | $0.22^{+0.12}_{-0.03}$ |
| B | $Y_{\rm bar}$ | $0.63^{+0.08}_{-0.04}$ | $0.85^{+0.03}_{-0.05}$ | $0.93^{+0.01}_{-0.02}$ | $0.98^{+0.01}_{-0.02}$ |
| | $Y_{\rm gas}$ | $0.42^{+0.07}_{-0.05}$ | $0.72^{+0.04}_{-0.05}$ | $0.82^{+0.02}_{-0.02}$ | $0.89^{+0.01}_{-0.03}$ |
| | $Y_{\rm hot}$ | $0.37^{+0.03}_{-0.03}$ | $0.67^{+0.02}_{-0.03}$ | $0.73^{+0.03}_{-0.03}$ | $0.64^{+0.08}_{-0.05}$ |
| | $Y_{\rm cold}$ | $0.04^{+0.06}_{-0.02}$ | $0.04^{+0.02}_{-0.01}$ | $0.09^{+0.02}_{-0.03}$ | $0.26^{+0.05}_{-0.11}$ |
| | $Y_{\rm star}$ | $0.21^{+0.04}_{-0.01}$ | $0.12^{+0.01}_{-0.01}$ | $0.10^{+0.01}_{-0.01}$ | $0.09^{+0.01}_{-0.01}$ |
| | $Z_{\rm tot}$ | $0.29^{+0.09}_{-0.06}$ | $0.25^{+0.05}_{-0.06}$ | $0.26^{+0.04}_{-0.02}$ | $0.20^{+0.04}_{-0.05}$ |
| C | $Y_{\rm bar}$ | $0.72^{+0.04}_{-0.07}$ | $0.90^{+0.02}_{-0.03}$ | $0.95^{+0.03}_{-0.02}$ | $0.99^{+0.01}_{-0.01}$ |
| | $Y_{\rm gas}$ | $0.53^{+0.03}_{-0.07}$ | $0.78^{+0.01}_{-0.03}$ | $0.85^{+0.03}_{-0.02}$ | $0.90^{+0.01}_{-0.01}$ |
| | $Y_{\rm hot}$ | $0.50^{+0.03}_{-0.06}$ | $0.74^{+0.01}_{-0.03}$ | $0.76^{+0.04}_{-0.03}$ | $0.65^{+0.08}_{-0.06}$ |
| | $Y_{\rm cold}$ | $0.03^{+0.01}_{-0.01}$ | $0.04^{+0.02}_{-0.01}$ | $0.08^{+0.03}_{-0.02}$ | $0.24^{+0.07}_{-0.07}$ |
| | $Y_{\rm star}$ | $0.18^{+0.02}_{-0.01}$ | $0.11^{+0.01}_{-0.01}$ | $0.10^{+0.01}_{-0.01}$ | $0.09^{+0.01}_{-0.01}$ |
| | $Z_{\rm tot}$ | $0.28^{+0.07}_{-0.05}$ | $0.27^{+0.06}_{-0.05}$ | $0.25^{+0.04}_{-0.02}$ | $0.21^{+0.08}_{-0.07}$ |
| D | $Y_{\rm bar}$ | $0.87^{+0.03}_{-0.04}$ | $0.93^{+0.01}_{-0.02}$ | $0.99^{+0.01}_{-0.01}$ | $1.00^{+0.01}_{-0.01}$ |
| | $Y_{\rm gas}$ | $0.69^{+0.04}_{-0.04}$ | $0.82^{+0.02}_{-0.02}$ | $0.88^{+0.01}_{-0.01}$ | $0.91^{+0.01}_{-0.01}$ |
| | $Y_{\rm hot}$ | $0.67^{+0.04}_{-0.05}$ | $0.79^{+0.01}_{-0.02}$ | $0.81^{+0.01}_{-0.01}$ | $0.68^{+0.03}_{-0.02}$ |
| | $Y_{\rm cold}$ | $0.02^{+0.01}_{-0.01}$ | $0.03^{+0.01}_{-0.01}$ | $0.07^{+0.01}_{-0.01}$ | $0.23^{+0.02}_{-0.03}$ |
| | $Y_{\rm star}$ | $0.17^{+0.02}_{-0.02}$ | $0.11^{+0.01}_{-0.01}$ | $0.11^{+0.01}_{-0.01}$ | $0.09^{+0.01}_{-0.01}$ |
| | $Z_{\rm tot}$ | $0.33^{+0.06}_{-0.04}$ | $0.28^{+0.04}_{-0.08}$ | $0.25^{+0.11}_{-0.08}$ | $0.16^{+0.08}_{-0.04}$ |

We provide here details on the values of the depletion parameters under investigation in different mass bins and at various radii (see Table A.1).

We also provide the best-fit parameters obtained from the fitting function in Eq. 8 (see Table A.2). As our findings are potentially useful for making predictions and comparisons with observational work, we confined our fitting produce to a radial range similar to that available for present and near-future X-ray observations and limited to the central regions of our anazlysis, from $0.5R_{500,c}$ to $2.5R_{500,c}$. The functional form is able to reproduce the behaviour of $Y_{\rm bar}$ well at all considered masses, as also shown by the $\tilde{\chi}^2$ and the values of the median and maximum deviation of the model from the data ($\tilde{e}$ and $e_{max}$, respectively) quoted in Table A.2. However, for the $Y_{\rm gas}$ and $Y_{\rm hot}$, we note that our fitting procedure gives less strong results than for the $Y_{\rm bar}$ case. We used the dispersion around the mean profile as weight to evaluate $\chi^2$.

**Table A.2.** Best-fit parameters and related standard errors for the functional form of Eq. 8 fitted to $Y_{\rm bar}$, $Y_{\rm gas}$, and $Y_{\rm hot}$.

| | $Y_{\rm bar}$ | $Y_{\rm gas}$ | $Y_{\rm hot}$ |
|---|---|---|---|
| $\alpha$ | $0.900 \pm 0.003$ | $0.733 \pm 0.004$ | $0.724 \pm 0.004$ |
| $\beta$ | $0.123 \pm 0.002$ | $0.223 \pm 0.003$ | $0.261 \pm 0.003$ |
| $\gamma$ | $0.233 \pm 0.005$ | $0.674 \pm 0.008$ | $0.756 \pm 0.009$ |
| $\delta$ | $-0.217 \pm 0.015$ | $-0.708 \pm 0.022$ | $-0.810 \pm 0.022$ |
| $\tilde{\chi}^2$ | 0.43 | 0.75 | 0.97 |
| $\tilde{e}$ | 2% | 4% | 5% |
| $e_{max}$ | 23% | 24% | 30% |

**Notes.** The values of the reduced $\chi^2$ ($\tilde{\chi}^2$) and the median and the maximum deviation of the model from the data ($\tilde{e}$ and $e_{max}$, respectively) are also quoted.

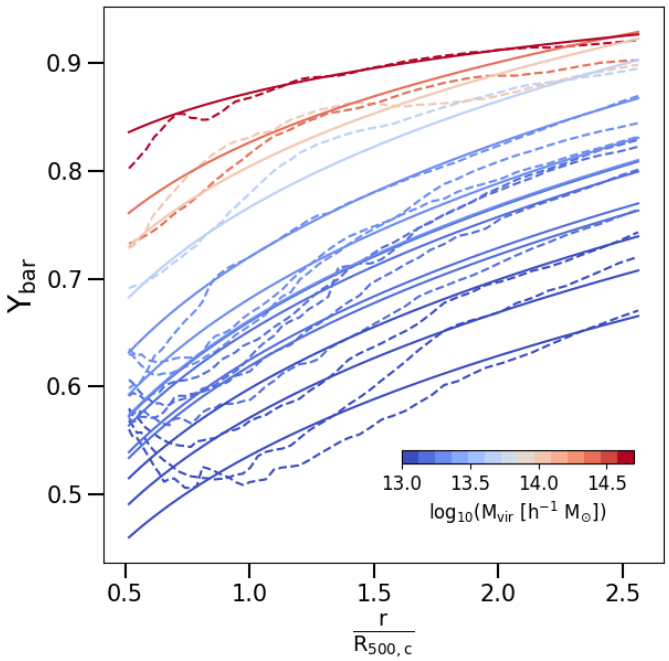


**Fig. A.1.** Radial profiles of baryon depletion, from $0.5R_{500,c}$ up to $2.5R_{500,c}$. The dashed lines represent the median profiles in each mass bin, according to the legend at the bottom-right corner. The solid lines are the fits performed according to the functional form of Eq. 8, with the same colour scale as the median profiles.